RSC Advances

PAPER

View Article Online
View Journal | View Issue

Cite this: *RSC Adv.*, 2024, **14**, 38539

Eco-friendly and facile one-step synthesis of manganese perovskite $(TMPEA)_2MnBr_4$ for high performance X-ray imaging

Yinke Liu, Chen Zhao, Dan Liu, Haibin Li, Jiwei Ren, Zhe Zheng and Yiying Zhao *

Inorganic–organic metal halogen perovskites, especially eco-friendly perovskites, have been intensively developed for X-ray imaging due to the high sensitivity, the low detection limit, and the high light yield. In this work, we successfully synthesized eco-friendly perovskite trimethylphenylammonium manganese(II) bromide ($(TMPEA)_2MnBr_4$) with a facile one-step method at room temperature and demonstrated its impressive potential for X-ray imaging. As-synthesized $(TMPEA)_2MnBr_4$ films have exhibited a high photoluminescence quantum yield (PLQY) of 83.18% at a peak wavelength of 521 nm with a huge Stokes Shift of 0.237 eV. The 70 μm perovskite film possesses a high light yield of 27 000 photons per MeV, spatial resolution of 10.2 lp mm^{-1}, and an impressive detection limit of 36.3 nGy_{air} s^{-1}. This work demonstrates the great potential of eco-friendly Mn-based perovskites and the novel easy fabrication method, which inspires further exploration in the field.

Received 8th October 2024
Accepted 29th November 2024

DOI: 10.1039/d4ra07220k

rsc.li/rsc-advances

1. Introduction

Recently, metal-halogen perovskite materials have been of great interest in a wide range of applications such as solar cells,[1] photodetectors,[2] light-emitting diodes (LEDs)[3] and scintillators because of their excellent photoelectronic properties. For instance, $CsPbBr_3$ nanocrystals have been applied to LEDs,[4] X-ray scintillation and X-ray imaging,[5] owing to the quantum confinement effect and strong X-ray absorption coefficient.[6] However, the toxicity[7] and the structural instability of conventional lead-based perovskites severely limit their further applications[8] in reality, and we require eagerly eco-friendly, high environmental stability, and high-performance scintillators.

Among the lead-free perovskites, Mn-based perovskites attracted rising research interest, due to their high quantum light yield, tunable emission wavelength in visible range, large stokes-shift, and better stability. Manganese (Mn)(II) has been widely adopted as dopant to effectively improve the photoluminescence quantum yields (PLQY) of the host system.[9,10] Recent research has shown that Mn(II) halide perovskites display an extremely high PLQY up to 99.96%.[11] The emission color of Mn(II) can be tuned from green to red *via* changing the coordination environment from the tetrahedral to octahedral complexes,[12] which indicates the promising potential applications such as multispectral X-ray imaging.[13,14] In addition, a 10% of Mn dopants could increase significantly the Stokes Shift of the BA_2PbBr_4 materials as large as 200 ms, exhibiting the great advantages of Mn-based perovskites for X-ray imaging.[15–17]

The Mn–Mn distance is one of the key factors to enlarge the Stokes Shift[18] and increase the PLQY of the Mn(II)-based host materials. A large Mn–Mn distance is preferred in general for reducing the fluorescence quenching.[19] The Mn–Mn distance can be adjusted *via* regulating the volume of A-site cation group in A_mMnX_4 ($m = 1, 2$) structure, which work as spacers between Mn atoms. However, cations with a large radius may cause the lattice distortion and decrease the energy transfer efficiency, resulting in a low PLQY.[20] For example, cation *N*-butyl-*N*-methyl-piperidinium ($[PP14]^+$) could reduce the PLQY of Mn-based perovskites to 55% compared with the 81% PLQY of the smaller cation *N*-butyl-*N*-methyl-pyrrolidinium ($[P14]^+$).[21] Therefore, it is important to choose an appropriate cation group to maintain the great advantage of Mn(II) based perovskites. Moreover, the room temperature process is favorable in the synthesis of Mn-based perovskites because the high temperature could reduce the PLQY of Mn-based scintillators.[22] Therefore, it is challenge to synthesize the high-performance Mn-based perovskite scintillators at room temperature, featured with a proper Mn–Mn distance.

Herein we demonstrated a promising Mn-based perovskite scintillator $(TMPEA)_2MnBr_4$ with a proper Mn–Mn distance of 8.64 Å for high performance X-ray imaging. An eco-friendly and facile one-step method was developed to synthesize the $(TMPEA)_2MnBr_4$ crystals at room temperature. The film exhibits a high PLQY of 83.18%, which is close to the current record of Mn-based perovskites[19] and even higher than that of some single crystals.[23,24] The spatial resolution of $(TMPEA)_2MnBr_4$ films is 10.2 lp mm^{-1} for the X-ray imaging, which is much

Institute of Materials, China Academy of Engineering Physics, Jiangyou, 621908, China. E-mail: zhaoyiying@caep.cn

higher than that of the dentistry CBCT (about 5 lp mm^{-1}). The high PLQY Mn-based perovskites and the one-step room temperature solution process developed in this work is inspiring and promising for the mass production of scintillators for high-performance X-ray imaging.

2. Results and discussions

2.1 Synthesis and structure characterization of $(TMPEA)_2MnBr_4$ perovskites

The $(TMPEA)_2MnBr_4$ perovskites were synthesized using a one-step solution method as shown in Fig. 1a. $(TMPEA)_2MnBr_4$ perovskites were formed by continuously stirring the dichloromethane (DCM) solution of (TMPEA) Br and $MnBr_2$ powders with a molar ratio of 2 : 1 until that the solution turned into fluorescent green. The as-synthesized green powders were obtained after the centrifugation of the above solution and the films was then fabricated on quartz substrates using the drop-casting method. The whole process only takes less than 10 minutes, which is much simple and fast compared with the solution temperature-lowering method (STL) for the single crystal growth and the evaporation method for most polycrystals.

The film fabricated in this work is 50 × 50 mm, which could be expanded to a larger area according to the demanding of various applications. The X-ray diffraction (XRD) patterns of the $(TMPEA)_2MnBr_4$ perovskites film in Fig. 1c were well matched with those of the standard PDF card of $(TMPEA)_2MnBr_4$ perovskites, which confirmed the successful formation of $(TMPEA)_2MnBr_4$ perovskites. The pristine $(TMPEA)_2MnBr_4$ perovskites belongs to a monoclinic space group of $C2/c$ with lattice constants of $a = 17.13$ Å, $b = 9.18$ Å and $c = 47.17$ Å.[19] As shown in Fig. 1b, Mn atoms coordinate with four adjacent Br atoms and form the $[MnBr_4]^{2-}$ tetrahedrons (T_d) and those tetrahedrons are separated with $[TMPEA]^+$ organic group cations, indicating that $(TMPEA)_2MnBr_4$ perovskites possess a green emission.[12] The closest Mn–Mn distance of 8.64 Å can be calculated from the crystal structure identified from single crystal X-ray diffraction,[19] which indicates the great probability of the high PLQY.[9,25] The scanning electron microscopy (SEM) image of the $(TMPEA)_2MnBr_4$ film in the inset of Fig. 1c shows that the film deposited on the glass substrate is relatively uniform and composed of particles of several micrometers. The structure characterizations indicate that we have successfully fabricated the pure phase of $(TMPEA)_2MnBr$ perovskites using a simple one-step solution method.

2.2 Optical properties of $(TMPEA)_2MnBr_4$ perovskites

Fig. 2 demonstrates the optical properties of $(TMPEA)_2MnBr_4$ films. Fig. 2a and b show the optical photographs of $(TMPEA)_2MnBr_4$ films under room light and UV light, respectively. The samples emitted green light under UV light, indicating the tetrahedral configuration of $[MnBr_4]^{2-}$ (ref. 26) in the $(TMPEA)_2MnBr_4$ films. The UV-vis absorption spectrum in Fig. 2c exhibits a strong absorption band between the 300 nm and 350 nm, which is mainly from the organic $[TMPEA]^+$ cations. The absorption bands of $[MnBr_4]^{2-}(T_d)$ were flooded over by that of $[TMPEA]^+$ cations in the UV-vis spectrum because of the large absorption cross-section of cations. The photoluminescence (PL) spectrum demonstrates that the $(TMPEA)_2MnBr_4$ film exhibits a narrow-band green emission peaked at 521 nm with a full width at half maximum (FWHM) of 48 nm. The excitation spectrum in Fig. 2d shows several peaks, corresponding to 363 nm, 376 nm, 438 nm, 454 nm, 463 nm, respectively. Then the Stokes Shift can be determined as the difference of the peak wavelength between the emission spectrum ($^4T_1 \rightarrow {}^6A_1$) and excitation spectrum ($^6A_1(S) \rightarrow {}^4T_1(G)$) with the value of 0.237 eV. The photophysics transition process in the $(TMPEA)_2MnBr_4$ films in Fig. 2d can be schematically illustrated using the Jablonski Diagram shown in Fig. 2e. The energy absorbed from the $[TMPEA]^+$ cations transferred to the Mn-centered tetrahedral $[MnBr_4]^{2-}$ (T_d) *via* the system crossing, where the excitons relaxed and emitted light. The theoretical calculation of the energy levels of the $[MnBr_4]^{2-}$ tetrahedrons[27,28] suggested that the emission corresponds to the transition of $^4T_1 \rightarrow {}^6A_1$ and the excitation corresponds to the transition of $^6A_1(S) \rightarrow {}^4E(D)$, $^6A_1(S) \rightarrow {}^4T_2(D)$, $^6A_1(S) \rightarrow {}^4A_1(G)/{}^4E(G)$, $^6A_1(S) \rightarrow {}^4T_2(G)$, and $^6A_1(S) \rightarrow {}^4T_1(G)$, respectively. The PLQY in Fig. 2f is high as up to 83.18% ± 0.40%, due to the effective energy transfer from $[TMPEA]^+$ to $[MnBr_4]^{2-}$ in the $(TMPEA)_2MnBr_4$ films and the reduced fluoresce quenching caused by a relatively large Mn–Mn distance.

The temperature dependent steady state PL spectra (TRPL) (80 K–280 K) were carried out to determine the exciton binding energy of the $(TMPEA)_2MnBr_4$ crystal. As shown in Fig. 2g, the PL peak intensity decreases and the corresponding FWHM broadens slightly with the increase of the temperature, which results from the enhanced excitons-phonons coupling effects at the elevated temperature.[29] The exciton binding energy stands for the stability against the dissociation of the hole electron pairs into free charge carriers, which could be carried out by the eqn (1),

$$I(T) = \frac{I_0}{1 + A\exp\left(-\frac{E_a}{k_B T}\right)} \quad (1)$$

where k_B is the Boltzmann constant, A is an applicable constant and $I(T)$ is the integrated PL intensity at temperature T. The exciton binding energy of the $(TMPEA)_2MnBr_4$ can be obtained as 27.48 meV from fitting the PL intensity with the Arrhenius model, as shown in Fig. 2h. To the best of our knowledge, no exciton binding energy of Mn-based scintillators can be founded in the literature. This exciton binding energy of the 0D $(TMPEA)_2MnBr_4$ perovskites is larger than that of 3D perovskites $CsPbBr_3$ (~18 meV).[30] The decay lifetime of the $(TMPEA)_2MnBr_4$ crystal is 372 μs obtained from fitting the decay curve of the time-resolved photoluminescence (TRPL) characterization in Fig. 2i, which is consistent with the previous reports.[31] We can see that $(TMPEA)_2MnBr_4$ is a promising scintillator with a high PLQY, big Stokes shift and a relatively large exciton binding energy, which shows the great potential for X-ray imaging.

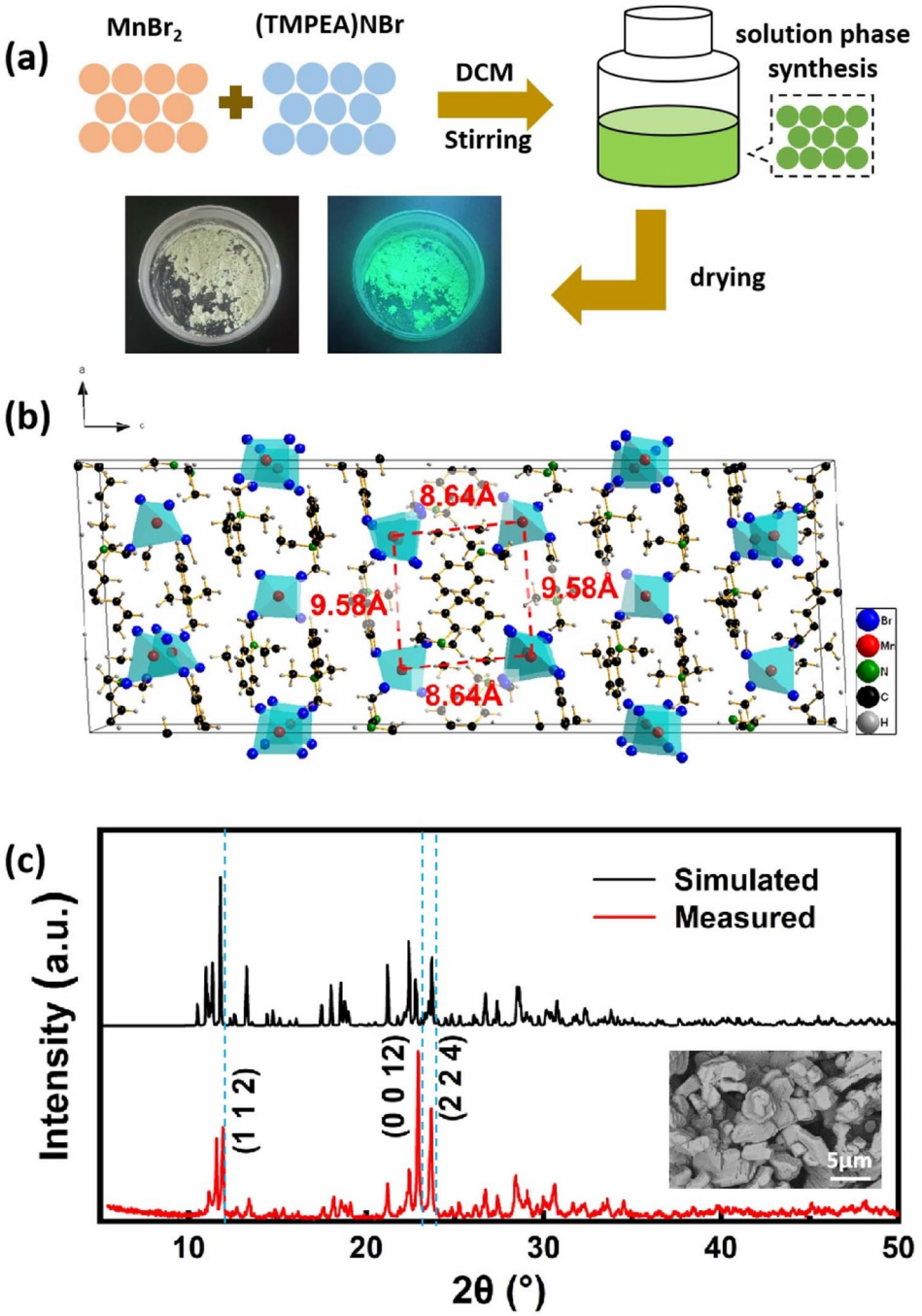

Fig. 1 (a) Schematic illustration of the Synthetic procedure and photos of $(TMPEA)_2MnBr_4$ powders (the one under UV light on the right side). (b) Schematic illustration of the crystal structure of $(TMPEA)_2MnBr_4$ (color scheme: Mn, red atoms; Br, blue atoms; C, black atoms; N, green atoms; H, gray atoms), marked with the Mn–Mn distance. (c) Measured XRD diagram and the standard PDF card of $(TMPEA)_2MnBr_4$ powders. (Inset) SEM image of the top-view of $(TMPEA)_2MnBr_4$ films drop-casted on the glass slide.

2.3 Radio-luminescence properties of $(TMPEA)_2MnBr_4$ perovskites

The radio-luminescence properties of $(TMPEA)_2MnBr_4$ films were characterized under different energy, dose rate, and irradiation time of X-rays, as shown in Fig. 3. The absorption coefficient curves of several typical X-ray detection materials at the photon energy from 10 keV to 1000 keV were plotted in Fig. 3a, where the $(TMPEA)_2MnBr_4$ exhibits a pretty good absorption capability across almost the whole energy region. Because of the existence of elements with large atomic number such as Br, the $(TMPEA)_2MnBr_4$ guarantee the X-ray stopping power ranging from 10 keV to 100 keV and exhibits a higher absorption coefficient of X-ray compared with Si in this energy region. The thickness of the $(TMPEA)_2MnBr_4$ film was measured

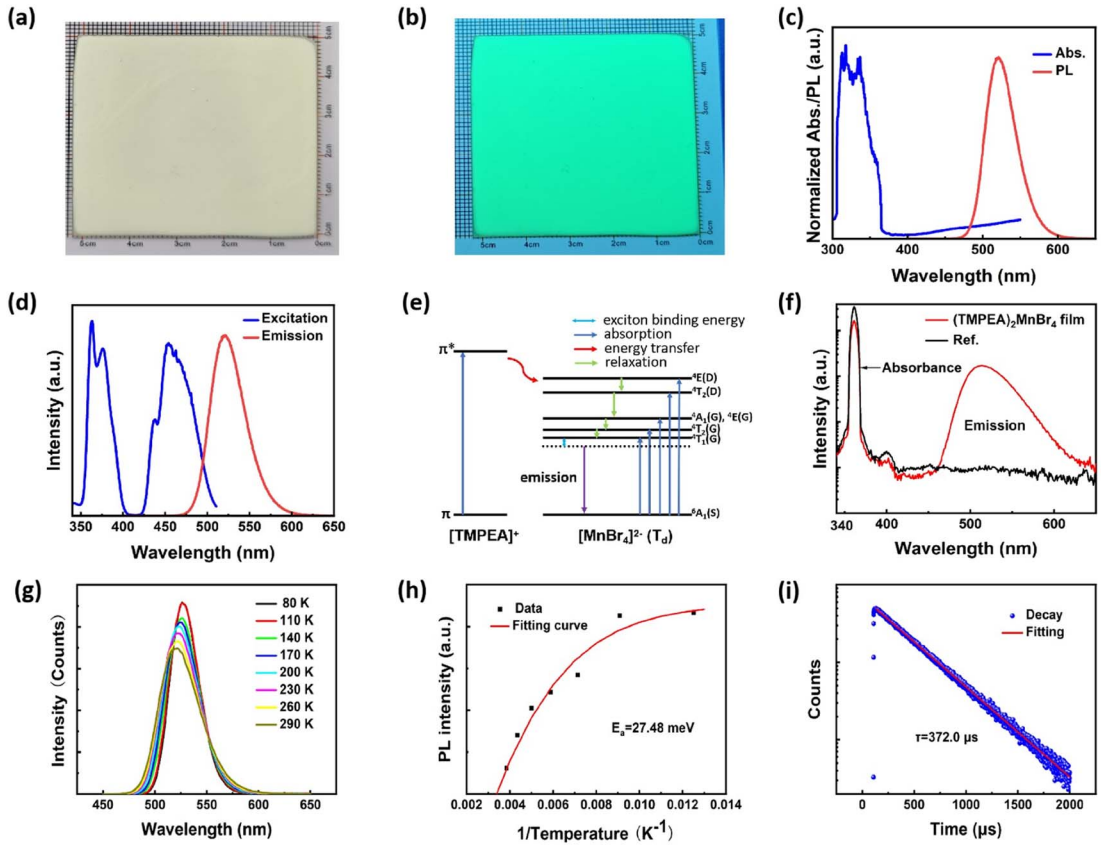

Fig. 2 Optical characterizations of $(TMPEA)_2MnBr_4$ films. Optical photographs under (a) room light and (b) UV illumination; (c) UV-vis absorption (blue line) and PL emission (red line) spectra; (d) excitation (blue line)-emission (red line) spectra; (e) Jablonski diagram denoted with the d^5 spectroscopic term split caused by the $[MnBr_4]^{2-}(T_d)$ tetrahedral crystal field; (f) absolute PL quantum yield (PLQY) measurements; (g) temperature dependent steady-state PL (TDPL) spectra (80 K–280 K); (h) exciton binding energy extracted by fitting the Arrhenius model; (i) time-resolved photoluminescence (TRPL) spectrum and the fitted lifetime.

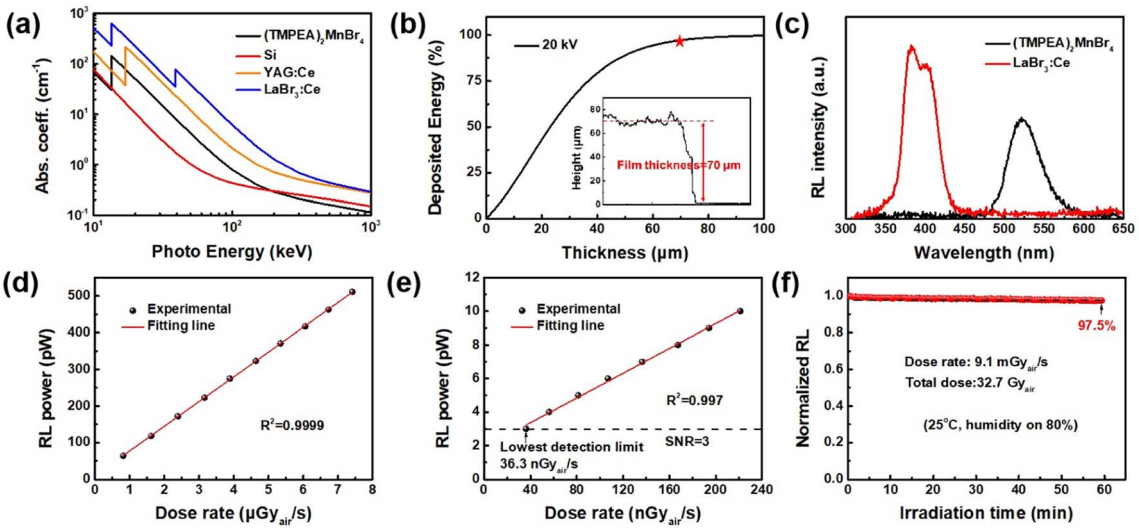

Fig. 3 X-ray radio-luminescence properties of $(TMPEA)_2MnBr_4$ films. (a) Absorption coefficients of $(TMPEA)_2MnBr_4$, $LaBr_3$, CsI:Tl, YAG:Ce and Si at various photon energy. (b) Deposited energy ratio in $(TMPEA)_2MnBr_4$ films with different thickness, (inset) thickness profile of $(TMPEA)_2MnBr_4$ film characterized by laser scanning confocal microscope. (c) RL intensity of $(TMPEA)_2MnBr_4$ film and $LaBr_3$ single-crystal scintillator. (d) Linear relationship between dose rate and RL power, showing a very high correlation coefficient. (e) Lowest detection limit at the signal noise ratio (SNR) of 3. (f) Operational stability of $(TMPEA)_2MnBr_4$ film under X-ray radiation with a dose rate of 9.1 mGy_{air} s^{-1}.

Table 1 The properties of Mn-scintillator in recent years

Mn-based scintillators	PLQY (%)	LoD (Gy_{air} s^{-1})	Light yield (photo per MeV)	Spatial resolution (lp mm^{-1})	Ref.
Cs_2ZnBr_4:Mn^{2+} polycrystalline	58.8	1.16 μ	15 600	5.06	35
$(C_{38}H_{34}P_2)MnBr_4$ single crystal	~95	72.8 n	~80 000	—	36
$C_4H_{12}NMnCl_3$	91.8	36.9 n	50 500	5	37
$(C_8H_{20}N)_2MnBr_4$ single crystals	85.1	24.2 n	24 400		
$[CH_3Ph_3P]_2MnBr_4$ glass	47.8	25.33 n	—	12.3	38
$(TBA)_2MnCl_4$ single crystal	99.96	381 n	21 000	5.6	11
$(TMPEA)_2MnBr_4$ polycrystalline	83.18	36.3 n	27 000	10.2	This work

using laser scanning confocal microscope. The thickness profile in the inset graph of Fig. 3b shows that the drop-casted $(TMPEA)_2MnBr_4$ film exhibits a uniform film thickness of 70 μm. As shown in Fig. 3b, the ratio of the deposited energy increases with the increase of the film thickness and a film of 70 μm can realize almost 100% energy deposition. The light yield of $(TMPEA)_2MnBr_4$ was calculated to be 27 000 photons per MeV by comparing with that of the commercial scintillator $LaBr_3$, as shown in Fig. 3c.

Fig. 3d shows the great linear relationship between the dose rate and the RL power of $(TMPEA)_2MnBr_4$ film in dose rate region below 8 μGy_{air} s^{-1}, which is much lower than that of medical examination (see standard GBZ 115-2023). The lowest detection limit can be obtained as 36.3 nGy_{air} s^{-1} by extrapolating the dose rate–RL power curve at the signal noise ratio of 3, as shown in Fig. 3e, which is even lower than that of single crystal Mn-based perovskites[32] in Table 1. The operation stability of $(TMPEA)_2MnBr_4$ film was characterized with a dose rate 9.1 mGy_{air} s^{-1} under a typical atmosphere environment at 25 °C with 80% humidity, as shown in Fig. 3f. The RL intensity only decreased slightly after an irradiation of 60 min with a total dose of 32.7 Gy_{air} (kept 97.5% RL intensity compared with initial value), showing a better irradiation hardness and stability compared with the commercial scintillator CsI:Tl.[33]

2.4 X-ray imaging performance of $(TMPEA)_2MnBr_4$ films

The X-ray imaging performance of $(TMPEA)_2MnBr_4$ films was characterized in Fig. 4. The X-ray imaging system is home-built and schematically illustrated in Fig. 4a, including an X-ray tube, an X–Y micro-positioner to hold the image object and the scintillator film, a mirror, and a camera. X-rays emitted from the X-ray tube illuminate the imaging object and the $(TMPEA)_2MnBr_4$ film from the top and the formed images are recorded by the camera.

The wire pair card with the maximal resolution of 30 lp mm^{-1} as shown in the inset of Fig. 4b, was employed to

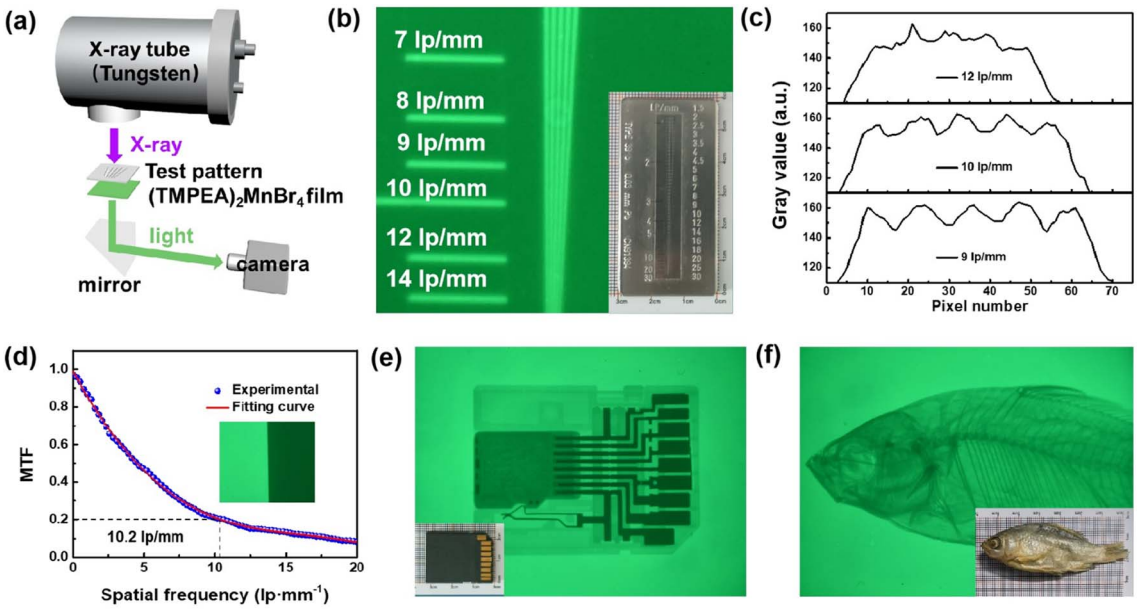

Fig. 4 X-ray imaging characterization of $(TMPEA)_2MnBr_4$ films. (a) Schematic diagram of the home-built X-ray imaging system. (b) X-ray images of the wire pair card (stainless steel), aiming to characterize the spatial resolution; (c) profiles of the gray values of the X-ray image of the wire pairs in (b); (d) Modulation transfer function (MTF) curve of X-ray images of the copper film using the slanted-edge method. (e) X-ray image of a SD card and (f) a dried fish.

characterize the spatial resolution of the $(TMPEA)_2MnBr_4$ film. The gray values of the X-ray image of the wire pair card were shown in Fig. 4c and the resolution can be obtained as 10 lp mm^{-1}, which is much higher than the commercial scintillators CsI:Tl[34] and other Mn-based scintillator single crystal[11] shown in Table 1. The spatial resolution can be determined as 10.2 lp mm^{-1} using the slanted-edge method at MTF = 0.2, as shown in Fig. 4d, which is consistent with the result of the wire pair method. The X-ray images of a SD card and a dried fish were shown in Fig. 4e and f, respectively, which are very clear and confirm the great X-ray imaging performance of the $(TMPEA)_2MnBr_4$ films.

The performance of Mn-based scintillators reported in previous work[11,33–36] have been summarized in Table 1. Compared with other scintillators, $(TMPEA)_2MnBr_4$ polycrystalline films demonstrated much better properties including the PLQY, the LoD and the Light yield than other Mn-based polycrystalline materials. $(TMPEA)_2MnBr_4$ polycrystalline films even demonstrate a higher spatial resolution and a lower LoD than that of some Mn-based single crystal scintillators. Considering the simple fabrication method, the $(TMPEA)_2MnBr_4$ is very promising for low-cost and high-performance X-ray imaging.

3. Conclusion

In summary, we developed an eco-friendly and facile one-step method to successfully synthesize 0D perovskites $(TMPEA)_2MnBr_4$ crystals at room temperature and demonstrated its promising potential for the high-performance X-ray imaging. The XRD characterization affirmed that the obtained powders are pure phase $(TMPEA)_2MnBr_4$ crystals with a monoclinic crystal structure. The optical characterizations indicate that the $(TMPEA)_2MnBr_4$ is efficient green phosphor with a peak emission wavelength at 521 nm, a long PL lifetime of 372 μs, and an impressive PLQY of 83.18%(±0.40%). The $(TMPEA)_2MnBr_4$ film exhibits a Stokes shift of 0.237 eV and the exciton binding energy of 27.48 meV, indicating the promising potential for X-ray imaging due to the neglectable self-absorption and the great stability. The $(TMPEA)_2MnBr_4$ film also exhibits a high light yield of 27 000 photons per MeV, a spatial resolution of 10.2 lp mm^{-1}, and an impressive detection limit of 36.3 nGy_{air} s^{-1}, which is close to the record of Mn-based scintillators. This promising Mn-based perovskites and the one-step room temperature solution process developed in this work is inspiring for the mass production of scintillators.

4. Experiments

4.1 Materials

(TMPEA)Br, $MnBr_2$, DCM (99%) were purchased from Sigma-Aldrich. Ethanol (99.7%) was purchased from Macklin. All the chemicals were used as received without further purification.

4.2 Synthesis of $(TMPEA)_2MnBr_4$

The $(TMPEA)_2MnBr_4$ was prepared by the facile one-step method at room temperature (25 °C) in DCM solution. $MnBr_2$ (0.214 g, 1 mmol) and (TMPEA)Br (0.432 g, 2 mmol) were dissolved in 10 ml of DCM. The solution was stirred until that light green colored precipitate present at the bottom of the vial. The precipitate was centrifuged at 11 000 rpm for 5 minutes and cleaned three times with ethanol. The obtained precipitate was used for the drop-casting process. The left $(TMPEA)_2MnBr_4$ was dried in vacuum for material characterization.

4.3 Characterization

XRD pattern were carried out by a DX-2700BH X-ray diffraction instrument, with a setup of Cu K_α radiation ($\lambda = 1.54184$ Å) at 40 kV and 30 mA and with step size of 0.02° and scan region from 5° to 50°. The reference patterns were simulated from CIF provided by database. SEM images data were recorded on a field emission scanning electron microscope ZEISS Gemini SEM 300 equipped. The UV-Visible absorption spectrum was measured by Shimadzu UV-1800 spectrometer using a 10 μm thickness film on glass plate and took a glass without film as the reference. The steady-state photoluminescence spectra were measured in Edinburgh instruments FLS 980, with an excitation wavelength of 362 nm and the time-resolved PL (TRPL) spectra were measured by FLS 980 using a 60 W μs flash lamp as an excitation light source. The temperature-dependent photoluminescence (TDPL) spectra were acquired by Edinburgh instruments FLS 1000 equipped with Orient-KOJI cryo77 cryogenic system in a temperature range from 80 K and 290 K with a distance of 10 K. The absolute PLQYs were recorded by Hamamatsu Photonics Quantaurus-QY Plus C13534-12. The film thickness and line width of mask were measured by the LEXT OLS5000 3D Measuring Laser Microscope (OLYMPUS).

4.4 Light yield calculation

The commercial scintillator $LaBr_3$ (63 000 photons per MeV) with a thickness of 10 mm was employed as ref. 38 and 39, and the light yield (LY) of the $(TMPEA)_2MnBr_4$ film (70 μm) was calculated according to the RL spectra by using the following equation reported in previous work,[39–41]

$$\frac{LY_{(TMPEA)_2MnBr_4}}{LY_{LaBr_3}} = \frac{\eta_{LaBr_3}\int I_{(TMPEA)_2MnBr_4}(\lambda)d\lambda \times S_{LaBr_3}}{\eta_{(TMPEA)_2MnBr_4}\int I_{LaBr_3}(\lambda)d\lambda \times S_{(TMPEA)_2MnBr_4}}$$

where η is the X-ray deposited energy percentage of scintillators, I is the RL intensity at different wavelength (λ), S is the irradiation area, respectively (X-ray intensity is assumed to be uniform across the whole tested irradiation area). The LY of $(TMPEA)_2MnBr_4$ film could then be calculated as 27 000 photos per MeV.

4.5 X-ray detection and imaging

An X-ray tube (Oxford, Apogee 5500 Series) with a tungsten target and working at 50 W (50 kV, 1.0 mA) was employed for X-ray imaging. RL spectra were acquired by Ocean optics, QE Pro spectrometer and optic-fiber coupled calibrated integrating sphere in Spectrum TEQ-PL system. The X-ray dose rate was calibrated by Radcal Accu-Gold digitizer equipped with an ionic chamber (10X6-180) dosimeter. The RL luminous stability was

determined by SpectrumTEQ-PL (Ocean Insight) quantum efficiency measurement system. The X-ray images were recorded by Nikon D750 with an AF-S Micro-NIKKOR 40 mm 1:1.28G lens.

Data availability

All the data for this article are available at Science Data Bank at **https://doi.org/10.57760/sciencedb.13364**.

Author contributions

This project was supervised by Yiying Zhao. Dan Liu and Yinke Liu designed the experiments. Yinke Liu synthesized the $(TMPEA)_2MnBr_4$ sample (powder and film) and characterized all the properties with the assistance of Chen Zhao. Haibin Li, and Jiwei Ren helped in the characterization of the X-ray imaging. Yinke Liu drafted this paper. Zhe Zheng and Yiying Zhao revised the paper.

Conflicts of interest

The authors declare no conflict of interest.

Acknowledgements

The Fundamental Research Funds of this project: National Natural Science Foundation of China (No. 12275243 and 12305403) and National Key R&D plan (2022YFE03170003).

References

1 M. A. Green, A. Ho-Baillie and H. J. Snaith, The emergence of perovskite solar cells, *Nat. Photon.*, 2014, **8**, 506.
2 X. Hu, X. Zhang, L. Liang, J. Bao, S. Li, W. Yang and Y. Xie, High-Performance Flexible Broadband Photodetector Based on Organolead Halide Perovskite, *Adv. Funct. Mater.*, 2014, **24**, 7373.
3 H. Cho, R. H. Friend and T. W. Lee, Overcoming the electroluminescence efficiency limitations of perovskite light-emitting diodes, *Science*, 2015, **350**, 1222.
4 L. Zhang, X. Yang, H. Sargent and J. You, Ultra-bright and highly efficient inorganic based perovskite light-emitting diodes, *Nat. Commun.*, 2017, **8**, 15640.
5 J. H. Heo and S. H. Im, High-Performance Next-Generation Perovskite Nanocrystal Scintillator for Nondestructive X-Ray Imaging, *Adv. Mater.*, 2018, **30**, 1801743.
6 L. Yang, H. Zhang, M. Zhou and L. X. Xu, High-stable X-ray imaging from all-inorganic perovskite nanocrystals under a high dose radiation, *J. Phys. Chem. Lett.*, 2020, **11**, 9203.
7 D. Yang, G. Zhang, R. Lai, Y. Cheng, Y. Lian, M. Rao, D. Huo, D. Lan, B. Zhao and D. Di, Germanium-lead perovskite light-emitting diodes, *Nat. Commun.*, 2021, **12**, 4295.
8 B. Park and S. I. Seok, Intrinsic Instability of Inorganic–Organic Hybrid Halide Perovskite Materials, *Adv. Mater.*, 2019, **31**, 1805337.
9 Q. Yao and X. T. Tao, Achieving a Record Scintillation Performance by Micro-Doping a Heterovalent Magnetic Ion in $Cs_3Cu_2I_5$ Single-Crystal, *Adv. Mater.*, 2023, **35**(44), 2304938.
10 N. Varnakavi, R. Rajavaram, K. Gupta, P. Cha and N. Lee, Scintillation Performance of Mn(II)-Doped $Cs_2NaBiCl_6$ Double Perovskite Nanocrystals for X-Ray Imaging Applications, *Adv. Opt. Mater.*, 2024, **12**(9), 2301868.
11 S. Cao and P. Feng, Ultrahigh Photoluminescence Quantum Yield Organic Manganese Halide Scintillator for X-ray Imaging, *ACS Appl. Opt. Mater.*, 2023, **1**, 623–632.
12 M. H. Choi and K. M. Ok, Green and Red Photoluminescent Manganese Bromides with Aminomethylpyridine Isomers, *Inorg. Chem.*, 2023, **62**(30), 12058–12066.
13 Y. Yang, Multispectral Large-Panel X-ray Imaging Enabled by Stacked Metal Halide Scintillators, *Adv. Mater.*, 2022, **34**, 2205458.
14 F. Yu, H. R. Zhang, X. W. Kong and C. Y. Yue, One-Dimensional Red Light–Emissive Organic Manganese(II) Halides as X-Ray Scintillators, *Inorg. Chem.*, 2024, **63**(39), 18146–18153.
15 W. Shao, Highly Efficient and Flexible Scintillation Screen Based on Manganese (II) Activated 2D Perovskite for Planar and Nonplanar High-Resolution X-Ray Imaging, *Adv. Opt. Mater.*, 2022, **10**, 2102282.
16 S. B. Xiao, S. Z. Zhang and L. J. Xu, Ultrahigh X-Ray Imaging Spatial Resolution Enabled by an 0D Mn(II) Hybrid Scintillator, *Adv. Funct. Mater.*, 2024, **34**(40), 2404003.
17 Z. J. Zhou, H. X. Meng, S. J. Liu and Q. Zhao, Highly Luminescent Nonclassical Binuclear Manganese(II) Complex Scintillators for Efficient X-ray Imaging, *Inorg. Chem.*, 2023, **62**(14), 5729–5736.
18 R. Zhou and P. Wu, Nanocrystals for large Stokes shift-based optosensing, *Chin. Chem. Lett.*, 2019, **30**, 1843–1848.
19 L. Mao, P. Guo and A. K. Cheetham, Design Principles for Enhancing Photoluminescence Quantum Yield in Hybrid Manganese Bromides, *J. Am. Chem. Soc.*, 2020, **142**, 13582–13589.
20 Y. Liu, New Insights into Mn−Mn Coupling Interaction-Directed Photoluminescence Quenching Mechanism in Mn^{2+}-Doped Semiconductors, *J. Am. Chem. Soc.*, 2020, **142**, 6649–6660.
21 L. Guo, Efficient modulation of photoluminescence by hydrogen bonding interactions between inorganic $[MnBr_4]^{2-}$ anions and organic cations, *Chem. Commun.*, 2019, **55**, 7303–7306.
22 J. H. Wei and D. B. Kuang, A Melt-Quenched Luminescent Glass of an Organic–Inorganic Manganese Halide as a Large-Area Scintillator for Radiation Detection, *Angew. Chem., Int. Ed.*, 2023, **62**, e202216504.
23 M. Li, Hybrid Metal Halides with Multiple Photoluminescence Centers, *Angew. Chem., Int. Ed.*, 2019, **58**(51), 18670–18675.
24 C. Jiang, $(Diisopropylammonium)_2MnBr_4$: a multifunctional ferroelectric with efficient green-emission and excellent gas sensing properties, *Chem. Commun.*, 2017, **53**, 5954.
25 G. Zhou, Z. Liu, J. Huang and M. S. Molokeev, Unraveling the Near-Unity Narrow-Band Green Emission in Zero-Dimensional Mn^{2+}-Based Metal Halides: A Case Study of

$(C_{10}H_{16}N)_2Zn_{1-x}Mn_xBr_4$ Solid Solutions, *J. Phys. Chem. Lett.*, 2020, **11**, 5956.

26 Y. L. Wei, J. Jing, Z. X. Wang and Y. Zhang, High quantum yield and unusual photoluminescence behaviour in tetrahedral manganese(II) based on hybrid compounds, *Inorg. Chem. Front.*, 2018, **5**, 2615.

27 R. Lazcano, Electronic structure and luminescence of $[(CH_3)_4N]_2MnX_4$ (X=Cl,Br) crystals at high pressures by time-resolved spectroscopy: Pressure effects on the Mn-Mn exchange coupling, *Phys. Rev. B*, 2009, **80**, 085115.

28 Q. Zhou, L. Dolgov, M. G. Brik and M. M. Wu, Mn^{2+} and Mn^{4+} red phosphors: synthesis, luminescence and applications in WLEDs. A review, *J. Mater. Chem. C*, 2018, **6**, 2652–2671.

29 Q. Zhou, Y. Y. Zhao and X. D. Han, Highly efficient copper halide scintillators for high-performance and dynamic X-ray imaging, *Nanoscale*, 2021, **13**, 19894–19902.

30 H. Yang, Y. Zhang, J. Pan, J. Yin, O. M. Bakr and O. F. Mohammed, Room-Temperature Engineering of All-Inorganic Perovskite Nanocrsytals with Different Dimensionalities, *Chem. Mater.*, 2017, **29**, 8978.

31 V. Morad, I. Cherniukh, L. Pöttschacher, Y. Shynkarenko, S. Yakunin and M. V. Kovalenko, Manganese (II) in Tetrahedral Halide Environment: Factors Governing Bright Green Luminescence, *Chem. Mater.*, 2019, **31**, 10161.

32 Y. Li, X. P. Ouyang and Q. Xu, Nanosecond and Highly Sensitive Scintillator Based on All-Inorganic Perovskite Single Crystals, *ACS Appl. Mater. Interfaces*, 2022, **14**, 1489–1495.

33 Y. Wang, X. Yin, T. E. Albrecht-Schmitt and S. Wang, Emergence of Uranium as a Distinct Metal Center for Building Intrinsic X-ray Scintillators, *Angew. Chem., Int. Ed.*, 2018, **57**, 7883–7887.

34 Q. Chen, H. Yang, W. Huang and X. Liu, All-inorganic perovskite nanocrystal scintillators, *Nature*, 2018, **561**, 88–93.

35 B. Su, K. Han and Z. Xia, Mn^{2+}-doped Cs_2ZnBr_4 scintillator for X-ray imaging, *J. Mater. Chem. C*, 2023, **11**, 8052–8061.

36 L. Xu, M. Worku and B. Ma, Highly efficient eco-friendly X-ray scintillators based on an organic manganese halide, *Nat. Commun.*, 2020, **11**, 4329.

37 Y. Su, P. Han, J. Hui and Y. Yang, Quantitative Dual-Energy X-ray Imaging Based on K-Edge Absorption Difference, *J. Phys. Chem. Lett.*, 2023, **14**(44), 10074–10079.

38 Z. Zhang, Z. He and D. B. Kuang, Organic–Inorganic Hybrid Mn-Based Transparent Glass for Curved X-Ray Scintillation Imaging, *Adv. Opt. Mater.*, 2023, **12**(11), 2302434.

39 R. Pani, M. N. Cinti, A. Fabbri, C. Orlandi, R. Pellegrini, R. Scafè and M. Colarieti-Tosti, Excellent pulse height uniformity response of a new $LaBr_3$:Ce scintillation crystal for gamma ray imaging, *Nucl. Instrum. Methods Phys. Res., Sect. A*, 2015, **787**, 46.

40 F. Cao, D. Yu, W. Ma, X. Xu, B. Cai, Y. M. Yang, S. Liu, L. He, Y. Ke and H. Zeng, Shining Emitter in a Stable Host: Design of Halide Perovskite Scintillators for X-ray Imaging from Commercial Concept, *ACS Nano*, 2020, **14**, 5183.

41 Q. Zhou, J. Ren, J. Xiao, L. Lei, F. Liao, H. Di, C. Wang, L. Yang, Q. Chen, X. Yang, Y. Zhao and X. Han, Highly efficient copper halide scintillators for high-performance and dynamic X-ray imaging, *Nanoscale*, 2021, **13**, 19894.